

Flux-Limited Diffusion Approximation Models of Giant Planet Formation by Disk Instability. II. Quadrupled Spatial Resolution

Alan P. Boss

Earth & Planets Laboratory, Carnegie Institution for Science, 5241 Broad Branch Road, NW, Washington, DC 20015-1305

aboss@carnegiescience.edu

ABSTRACT

While collisional accumulation is nearly universally accepted as the formation mechanism of rock and ice worlds, the situation regarding gas giant planet formation is more nuanced. Gas accretion by solid cores formed by collisional accumulation is the generally favored mechanism, but observations increasingly suggest that gas disk gravitational instability might explain the formation of at least the massive or wide-orbit gas giant exoplanets. This paper continues a series aimed at refining three-dimensional (3D) hydrodynamical models of disk instabilities, where the handling of the gas thermodynamics is a crucial factor. Boss (2017, 2019, 2021) used the β cooling approximation (Gammie 2001) to calculate 3D models of disks with initial masses of $0.091 M_{\odot}$ extending from 4 to 20 au around $1 M_{\odot}$ protostars. Here we employ 3D flux-limited diffusion (FLD) approximation models of the same disks, in order to provide a superior treatment of disk gas thermodynamics. The new models have quadrupled spatial resolution compared to previous 3D FLD models (Boss 2008, 2012), in both the radial and azimuthal spherical coordinates, resulting in the highest spatial resolution 3D FLD models to date. The new models continue to support the hypothesis that such disks can form self-gravitating, dense clumps capable of contracting to form gas giant protoplanets, and suggest that the FLD models yield similar numbers of clumps as β cooling models with $\beta \sim 1$ to ~ 10 , including the critical value of $\beta = 3$ for fragmentation proposed by Gammie (2001).

Subject headings: accretion, accretion disks – hydrodynamics – instabilities – planets and satellites: formation – protoplanetary disks

1. Introduction

The determination that the frequency of Earth-like planets is in the range of 0.37 to 0.88 planets per main-sequence dwarf star (Bryson et al. 2021) is certainly one of the most astonishing triumphs of modern astronomy, with consequent implications for the probability of habitable and inhabited exoplanets throughout the galaxy. The incredible success of the Kepler mission (Borucki et al. 2010; Koch et al. 2010) in achieving this landmark determination has proven that the basic scenario for the formation of our solar system, the collisional accumulation of increasingly larger solid bodies (Wetherill 1990, 1996), applies equally well throughout our galaxy. While the focus of theoretical modeling of collisional accumulation has evolved to include novel processes such as streaming instabilities (e.g., Youdin & Goodman 2005; Yang et al. 2017) and pebble accretion (e.g., Chambers 2018; Matsumura et al. 2021), the basic scenario of building exoplanets from the ground up has remained as the leading formation mechanism.

Within the context of the collisional accumulation scenario, the formation of the gas and ice giant planets is hypothesized to also proceed from the bottom up, through the accretion of protoplanetary disk gas by solid cores formed by collisional accumulation. Once these cores reach masses roughly ten times that of the Earth, Mizuno (1980) showed that their extended gaseous atmospheres would become unstable toward inward collapse, leading to sustained accretion of additional disk gas and growth to Jupiter-like masses. There is, however, an alternative for gas giant planet formation, the top-down mechanism of gas disk gravitational instability (Boss 1997), where a massive protoplanetary disk forms spiral arms which grow and interact, resulting in the formation of self-gravitating clumps of disk gas and dust that could contract to form gas giant protoplanets. While disk instability is not generally favored over core accretion (e.g., see Helled et al. 2014), observational evidence has suggested a role for disk instability in the formation of massive and wide-orbit gas giant planets, as summarized in Boss (2017, 2019, 2021). The metallicity study of Adibekyan (2019) similarly found a role for disk instability in the formation of high mass exoplanets. A recent study of the metallicities of stars with massive planets (Mishenina et al. 2021) found $[\text{Fe}/\text{H}]$ ratios ranging from -0.3 to 0.4, i.e., ranging from metal-poor to metal-rich, compared to the solar ratio.

Gas giant exoplanets are considerably easier to detect than lower mass planets, but Figure 1 shows that a complete theory of planetary system formation must take into account the formation mechanisms of gas giants: they are not rare objects whose existence can be ignored. In fact, a recent demographic study of Doppler exoplanet detections for FGKM stars (Fulton et al. 2021) has concluded that giant planets have an occurrence rate of about 14% for semi-major axes of 2 au to 8 au and a rate of about 9% for semi-major axes of 8

au to 32 au. Given that these occurrence rates are considerably lower than those of Earth-like planets with radii between 0.5 and 1.5 R_{\oplus} (Bryson et al. 2021), and of the even more abundant super-Earths and sub-Neptunes with larger radii (Kunimoto & Matthews 2020), it is surprising that Figure 1 shows so many gas giants have been detected. The papers in this series attempt to help explain the formation mechanism(s) of this significant exoplanet population.

Boss (2001) calculated the first disk instability models with 3D radiative transfer hydrodynamics (RHD), finding fragmentation in disks that previously had been modeled as being locally isothermal. Gammie (2001) hypothesized that a gas disk gravitational instability would lead to fragmentation if the parameter β was less than 3, where $\beta = t_{cool}\Omega$, with t_{cool} being the disk cooling time and Ω being the local angular velocity. Durisen et al. (2007) reviewed 3D RHD models where fragmentation did or did not occur, noting the importance of various numerical factors for the outcome, such as spatial grid resolution, the use of flux limiters for radiative transfer in the diffusion approximation, the accuracy of the gravitational potential solver, and the disk gas thermodynamics controlling the heating and cooling processes. Boss (2017) discussed the variety of results obtained from both RHD and β cooling models of disk instability, with the latter models finding critical values for fragmentation ranging from $\beta \sim 3$ to as high as ~ 30 , with the critical value often depending on the spatial resolution used, as was also found in the 3D β cooling simulations of Brucy & Hennebelle (2021). Deng et al. (2021) found that $\beta = 3$ was sufficient to trigger disk fragmentation in their 3D magnetohydrodynamic models of protoplanetary disk evolution using a particle-based code.

The present paper presents a set of FLD calculations of the same initial disk models considered in the FLD models of Boss (2008, 2012) and in the β cooling models of Boss (2017). The Boss (2008, 2012) models were limited in time compared to the present models, and more importantly, were restricted to a maximum of 100 radial (r) and 512 azimuthal (ϕ) grid points, whereas the new models quadrupled both of these maxima, up to 400 in radius and 2048 in azimuth. [The vertical resolution was unchanged, as the grid is compressed to the midplane in either case.] Along with the β cooling models of Boss (2021), these are the highest spatial resolution grid models ever run with the EDTONS code. The models thus seek to approach the ideal of converging to the continuum limit of infinite spatial resolution and to further determine the ability of the disk instability mechanism to form dense clumps capable of becoming gas giant planets.

2. Numerical Methods and Flux-Limiter Derivation

The numerical code is the same code as that used in the many previous studies of gas disk gravitational instability by the author (e.g., Boss 2008, 2012, 2017, 2019, 2021). The EDTONS code solves the three-dimensional equations of hydrodynamics and the Poisson equation for the gravitational potential, with second-order-accuracy in both space and time, on a spherical coordinate grid (Boss & Myhill 1992). The code uses van Leer type hydrodynamic fluxes and has undergone extensive testing (e.g., Boss & Myhill, 1992; Boss 2007, 2009). The five hydrodynamic equations are solved in conservation law form using explicit time differences.

With the exception of the recent β cooling models of Boss (2017, 2019, 2021), all of the EDTONS disk instability models since Boss (2001) have employed radiative transfer in the diffusion approximation. This involves solving the hydrodynamic equation which determines the evolution of the specific internal energy E :

$$\frac{\partial(\rho E)}{\partial t} + \nabla \cdot (\rho E \mathbf{v}) = -p \nabla \cdot \mathbf{v} + \nabla \cdot \left[\frac{4}{3\kappa\rho} \nabla(\sigma T^4) \right],$$

where ρ is the total gas and dust mass density, t is time, \mathbf{v} is the velocity of the gas and dust (considered to be a single fluid), p is the gas pressure, κ is the Rosseland mean opacity, σ is the Stefan-Boltzmann constant, and T is the gas and dust temperature. Boss (1984) describes in detail the equations of state used for the gas pressure, the specific internal energy, and the dust grain opacity relation.

Boss (2008) presented the following derivation of a flux-limiter that could be used in concert with the EDTONS diffusion approximation code, which is exact only at high optical depths. A flux-limiter can be employed to handle low optical depth regions (e.g., Bodenheimer et al. 1990). The purpose of a flux-limiter is to enforce the physical law that in low optical depth regions the ratio of the radiative flux \vec{F} to the radiative energy density e_r cannot exceed the speed of light c , i.e., $|\vec{F}| \leq c e_r$. Bodenheimer et al. (1990) adopted a prescription for enforcing this constraint based on the flux-limiter proposed by Levermore & Pomraning (1981) for the situation where scattering of light is negligible.

As noted by Boss (2008), the EDTONS diffusion approximation code is derived from a code that handles radiation transfer in the Eddington approximation (Boss 1984; Boss & Myhill 1992). In this code, the energy equation is solved along with the mean intensity equation, given by

$$\frac{1}{3} \frac{1}{\kappa\rho} \nabla \cdot \left(\frac{1}{\kappa\rho} \nabla J \right) - J = -B$$

where J is the mean intensity and B is the Planck function ($B = \sigma T^4/\pi$). The mean intensity J is related to the radiative energy density e_r by $J = ce_r/4\pi$, while the net flux vector \vec{H} is given by $\vec{H} = \vec{F}/4\pi$. Hence, the statement of physical causality $|\vec{F}| \leq ce_r$ is equivalent to $|\vec{H}| \leq J$. The Eddington approximation version of the code does not calculate \vec{H} directly, but rather $\nabla \cdot \vec{H}$, as this quantity is used in the code to calculate the time rate of change of energy per unit volume due to radiative transfer, L , through

$$L = -4\pi \nabla \cdot \vec{H} = \frac{4\pi}{3} \nabla \cdot \left(\frac{1}{\kappa\rho} \nabla J \right)$$

in optically thick regions (Boss 1984). Hence, it is convenient to apply the physical causality constraint $|\vec{H}| \leq J$ in another form. Using the equation for L , one finds

$$\vec{H} = -\frac{1}{3\kappa\rho} \nabla J.$$

The constraint $|\vec{H}| \leq J$ then becomes

$$\left| \frac{4\pi}{3\kappa\rho} \nabla J \right| \leq 4\pi J.$$

This constraint is then evaluated in a convenient but approximate manner by effectively taking the divergence of both sides of this equation, resulting in a constraint on L that

$$|L| = \left| \frac{4\pi}{3} \nabla \cdot \left(\frac{1}{\kappa\rho} \nabla J \right) \right| \leq |4\pi \nabla \cdot \vec{J}|,$$

where \vec{J} is a pseudovector with J as components in all three directions. In the diffusion approximation, $J = B$. In practice, then, L is calculated for each numerical grid point, and if $|L|$ exceeds $|4\pi \nabla \cdot \vec{J}|$, L is set equal to $|4\pi \nabla \cdot \vec{J}|$ but with the original sign of L (i.e., preserving the sense of whether the grid cell is gaining or losing energy through radiative transfer). This constraint on L (Boss 2008) is thus a suitable replacement for the Levermore & Pomraning (1981) flux-limiter.

3. Numerical Spatial Resolution and Initial Conditions

The numerical grid has $N_r = 100, 200,$ or 400 uniformly spaced radial grid points, $N_\theta = 23$ theta grid points, distributed from $\pi/2 \geq \theta \geq 0$ and compressed toward the disk midplane, and $N_\phi = 512, 1024,$ or 2048 uniformly spaced azimuthal grid points. The radial grid extends from 4 to 20 au, with disk gas flowing inside 4 au being added to the central protostar, whereas that reaching the outermost shell at 20 au loses its outward radial momentum but remains on the active hydrodynamical grid. The gravitational potential is obtained through a spherical harmonic expansion, including terms up to $N_{Ylm} = 48$ for all spatial resolutions. The central protostar wobbles to preserve the center of mass of the entire system.

Starting with initial grid resolutions of $N_r = 100$ and $N_\phi = 512$, the r and ϕ numerical resolutions are doubled and then quadrupled when needed to avoid violating the Jeans length (e.g., Boss et al. 2000) and Toomre length criteria (Nelson 2006). These criteria were developed to avoid spurious fragmentation caused by inferior spatial grid resolution in Eulerian hydrodynamics simulations of disk instability. The Jeans length criterion has also been found recently to apply to Lagrangian hydrodynamic schemes when studying gravitational fragmentation (Yamamoto et al. 2021). As in Boss (2017, 2019, 2021), if either criterion is violated, the calculation stops, and the data from a time step prior to the criterion violation is used to double the spatial resolution in the relevant direction by dividing each cell into half while conserving mass and momentum.

Even with quadrupled spatial resolution, in some models dense clumps formed that violated the Jeans or Toomre length criteria at their density maxima. In that case, the calculation is halted and restarted from a previously stored time step when these two criteria are not yet violated. The offending high density cell is drained of 90% of its mass and momentum, which is then inserted into a virtual protoplanet (VP, Boss 2005), as in Boss (2017, 2019, 2021). VPs are only created when a clump becomes so dense as to violate the Jeans or Toomre length criteria and their creation is required in order to continue the calculation with numerical rigor. The VPs acquire circumplanetary structures that orbit along with the VPs (e.g., Figure 2a shows two VPs embedded in bright red, high density disk gas at between 9 o'clock and 10 o'clock for model fldA). Such configurations are considered to be only VPs, in the sense of the counts tabulated in Table 1; note that the clumps in Table 1 do not contain embedded VPs. The VPs orbit in the disk midplane, subject to the gravitational forces of the disk gas, the central protostar, and any other VPs, while the disk gas is subject to the gravity of the VPs. VPs gain mass at the rate (Boss 2005, 2013) given by the Bondi-Hoyle-Lyttleton (BHL) formula (e.g., Ruffert & Arnett 1994), as well as the angular momentum of any accreted disk gas. Any VPs that reach the the inner or

outer boundaries are removed from the calculation. VPs are analogous to the sink particles used in certain Eulerian hydro codes, such as the FLASH (Fryxell et al. 2000) and enzo (<https://enzo-project.org/index.html>) adaptive mesh refinement (AMR) codes.

In the Boss (2017, 2019, 2021) models, the initial gas disk density distribution is that of an adiabatic, self-gravitating, thick disk with a mass of $M_d = 0.091M_\odot$, in near-Keplerian rotation around a solar mass protostar with $M_s = 1.0M_\odot$ (Boss 1993). The initial density distribution has a small (1%) nonaxisymmetric perturbation, while the initial temperature distribution is axisymmetric. The initial radial temperature profile decreases from a temperature of 600 K at the inner boundary at 4 au to a specified initial outer disk temperature T_{oi} at a distance of ~ 6 au, as shown in Figure 1 of Boss (2019). Table 1 lists the initial temperatures in outer disks for the eight new FLD models, which range from 40 K to 180 K, the same as the range explored in the β cooling models of Boss (2017). These temperatures result in initial minimum Toomre Q values for the disks ranging from $Q_{min} = 1.3$ to $Q_{min} = 2.7$, i.e., from marginally unstable to relatively stable. Figure 2 of Boss (2017) shows that the initial Q value is ~ 9.5 at 4 au, but drops steeply to close to the minimum value beyond ~ 10 au.

It is important to note that the disk temperatures in the Boss (2017) β cooling models were not allowed to decrease below their initial values, in order to provide continuity with all of the previous disk instability models with the EDTONS code. The same numerical assumption was employed in the current FLD models. As noted by Boss (2017), this means that initially high Q disks cannot become gravitationally unstable solely due to cooling to lower temperatures than that of the initial disk, and can only become more gravitationally unstable by transporting disk mass in such a manner that the local disk surface density increases, thereby lowering Q locally. In contrast, in the β cooling models of Boss (2019, 2021) the disk temperature is allowed to cool below the initial value, to as low as 40 K.

4. Results

Figures 2 and 3 display the the final midplane density and temperature fields for a representative sample of four of the eight models listed in Table 1, models fldA and fldC in Figure 2, and models fldF and fldH in Figure 3. The initial outer disk temperatures for these four models are 40 K, 70 K, 100 K, and 180 K, respectively. As stated above, it is important to note that in these new models, as well as in the β cooling models of Boss (2017), the minimum disk temperature at any point is defined to be the initial temperature. Hence the disks are allowed to become hotter, but cannot cool down below their initial temperature radial profiles. This explains the dramatically different behavior seen in Figures 2 and 3.

Model fldA, with an initial $Q_{min} = 1.3$, is the most gravitationally unstable from the start, and as a result forms the familiar pattern of spiral arms and dense clumps in less than 200 yrs. Model fldC, somewhat more gravitationally stable to start with an initial $Q_{min} = 1.7$, still manages to form well-defined spiral arms and a few clumps by 260 yrs. The situation has clearly deteriorated for the models in Figure 3, where initial Q_{min} values of 2.1 and 2.7 characterize models fldF and fldH, respectively. Model fldF is able to form only weak spiral arm features, whereas model fldH settles for forming a shallow ring with no distinct clumps, as a result of starting from a Toomre-stable initial configuration. Note though that model fldF was able to form a single VP during its evolution, and the VP survived in orbit through to the final time of 287 yrs.

Figures 2 and 3 show that the dense spiral arms are accompanied by disk gas temperatures that rise well above the initial values as a result of compressional heating of the disk gas to form the spiral features. The vertical midplane optical depths in the initial models range from $\sim 10^4$ at the inner disk boundary to $\sim 10^2$ at the outer disk boundary, meaning that the compressional heating cannot be quickly radiated away from the disk’s surface. The flux-limited diffusion approximation is intended to provide a superior treatment of the proper handling of disk thermodynamics than that provided by the classic β cooling approximation. Given that increasing disk temperatures produce gas pressure gradients that resist clump formation and survival, the fact that well-defined spiral arms and dense clumps still form in these high-spatial resolution flux-limited diffusion approximation models yields strong support for the hypothesis that some gas giant protoplanets may form from a phase of disk gas gravitational instability in a sufficiently massive and cool disk.

Figure 4 presents a direct comparison between the compressional heating in these FLD models and the previous β cooling models by showing the results for models that both started with $Q_{min} = 1.3$ and an outer disk temperature of 40 K. Figure 4 displays the radial temperature and density profiles through a FLD model, namely model fldA’s clump 3 (Table 1), compared to a clump from model 1.3-3 (Table 1 in Boss 2017) with $\beta = 3$ cooling. The present FLD models have twice the radial grid resolution as the Boss (2017) β cooling models, but in both cases the clumps at ~ 10 au are defined by sharply peaked profiles in both the midplane density and the temperature fields. In both cases, the vertical optical depth at the midplane at the clump centers is greater than 10^3 , i.e., highly optically thick. Figure 4 shows the clump in the β cooling model has reached a maximum density ~ 3 times higher than the fldA clump, yet has a comparable peak temperature of ~ 100 K. This shows that the choice of $\beta = 3$ cooling errs somewhat on the side of cooling the disk faster than the FLD models predict should be the case. As we shall see below, however, while no single value of β is able to match the FLD model results, Figure 4 shows that a value of $\beta = 3$ does not produce grossly disparate results compared to the comparable FLD model. A similar

result was found by Szulágyi et al. (2017), whose Figure 7 compares the radial temperature gradients around clumps formed in a model with FLD with one with local cooling, similar to β cooling: both treatments yielded similar clump temperature gradients, with a peak temperature of ~ 115 K in the FLD model.

Table 1 lists the key results for all of the models: the final times reached, the final spatial resolutions in r and ϕ , the final number of VPs and of strongly and weakly gravitationally bound clumps present at the final time, and the sum of those two ($N_{VP} + N_{clumps} = N_{total}$). As described in Boss (2021), the number of clumps (N_{clumps}) was assessed by searching for dense regions with densities greater than 10^{-10} g cm $^{-3}$. For clumps of this density or higher, the free fall time is 6.7 yrs or less, considerably less than the orbital periods, implying that such clumps might be able to survive and contract to form gaseous protoplanets. Orbital periods of the disk gas range from 8.0 yrs at the inner edge (4 au) to 91 yrs at the outer edge (20 au). The final times reached ranged from 189 yrs to 1822 yrs, indicating that the models spanned time periods long enough for many revolutions in the inner disk and multiple revolutions in the outer disk. The models required over 4.5 years to compute, with each model running on a separate, single core of the Carnegie memex cluster at Stanford University.

Table 2 displays the clump properties for the eight new models upon which the numbers of clumps in Table 1 were assessed. As described by Boss (2021), the clumps are classified as either unbound (U), weakly (W), or strongly (S) self-gravitating, depending on whether the clump mass is less than (U), greater than (W), or more than 1.5 times (S) the Jeans mass for self-gravitational collapse of a cloud with the average temperature of the clump. The Table 2 evaluations were performed at the conclusions of the calculations. The Jeans mass is the mass of a sphere of uniform density gas with a radius equal to the Jeans length, where the Jeans length is the critical wavelength for self-gravitational collapse of an isothermal gas (e.g., Boss 1997, 2005). In cgs units, the Jeans mass is given by $1.3 \times 10^{23} (T/\mu)^{3/2} \rho^{-1/2}$, where T is the gas temperature, ρ the gas density, and μ the gas mean molecular weight, conservatively taken here to be 2.0 for molecular hydrogen gas. The volume-averaged clump temperature and the volume-averaged clump density are used to compute the Jeans masses in Table 2, conservatively producing higher Jeans masses than would be the case if the maximum clump density was used (cf., Boley et al. 2010). The clumps are defined to include all cells contiguous with the maximum density cell with a density no more than a factor of 10 times smaller. Clumps with masses exceeding the Jeans mass are capable of self-gravitational collapse on a time scale given by the free fall time, t_{ff} , where $t_{ff} = (3\pi/32G\rho)^{1/2}$ and G is the gravitational constant. All of these clumps have a maximum densities higher than 10^{-10} g cm $^{-3}$ (Table 2), implying collapse times shorter than a free fall time of 6.7 yr, and thus considerably shorter times than their orbital periods.

The Jeans mass is of course merely an approximation for estimating clump properties, used in part here to ensure uniformity with the analysis of the previous papers in this series (e.g., Boss 2019, 2021). The Jeans mass definition is based on the analysis of the gravitational instability of a linear wave in a uniform density gas, and then taking half that unstable wavelength (the Jeans length) as being the radius of a sphere, yielding the Jeans mass, clearly itself an approximation to a more complicated situation. The clumps formed in these models tend to be segments of spiral arms, often with irregular shapes, given the definition here of a clump being all contiguous cells within a factor of 10 of the maximum density. The heights of the clumps above the disk midplane, as defined by this factor of 10 decrease, are comparable to their radial extents in the disk midplane. Thus the clumps are not strongly flattened, but rather sausage-like in cross-section. Because of their irregular shapes, a simple formula for their self-gravity does not exist, unlike the case of a uniform density sphere, where the self-gravity is easily calculated ($-3GM^2/5R$, for mass M and radius R). This makes it difficult to compute the ratio of their thermal energy to their self-gravitational energy as an alternative to the simple Jeans mass estimates used here and in past papers (e.g., Boss 2019, 2021). A related approach to estimating clump masses and properties was performed by Boley et al. (2010) for their SPH models of disk fragmentation at distances greater than 50 au, using both the Jeans mass for a sphere and the Toomre mass for an unstable spiral arm.

While it would be interesting to continue these calculations further in time to continue to follow the evolution of the clumps and the VPs, that is not the purpose of this paper, which is to study the initial phases of clump formation at unprecedented spatial resolution. Boss (2013) followed the evolution of VPs in a gravitationally unstable disk, and found that Jupiter-mass VPs could orbit stably for as long as ~ 4000 yrs. As an example of clump evolution in the present models, model fldB produced a stable clump (#1 in Tables 2 and 3) which formed and orbited for one complete revolution by the time that the model was terminated and the clump’s properties were evaluated. Model fldB required 1.5 yrs of CPU time before this clump formed, and another 3 yrs to complete the final orbit, for a total of 4.5 yrs of computer time. The final 1/4 of its orbit required 2 yrs, as that was when the highest spatial resolution was required. Hence, in order to compute fldB’s clump #1 forward another complete orbit at the current rate would require another 8 yrs of computation. This estimate also ignores the fact that as the clump continues to slowly contract and evolve, it may well violate the Jeans or Toomre length criteria and require either the insertion of a VP or even higher spatial resolution. The latter would further slow the computation. VPs are a more promising means for studying the orbital evolution of bound clumps.

5. Discussion

Figure 5 displays the masses and semi-major axes of the gravitationally bound clumps and VPs from Table 3, compared to the gravitationally bound clumps from Boss (2021), where β cooling was used rather than the flux-limited diffusion approximation. Boss (2021) employed the same high spatial resolution as the present models, and so Figure 5 contrasts the difference between the FLD approximation and the β cooling approximation at an equivalent spatial resolution. It can be seen that the clump masses produced are similar in the two cases, but that the semi-major axes of the FLD clumps are from ~ 5 au to ~ 11 au, while those for β cooling are from ~ 8 au to ~ 18 au. This is a result of several other differences between the two sets of models. First, the FLD models did not allow the disk temperature to drop below the initial radial profile, whereas the β cooling models were allowed to cool down to 40 K. Second, the FLD models started from initial disks with a range in outer disk temperatures, up to 180 K for model fldH. The β cooling models all started from the same Toomre-stable outer disk temperature of 180 K, but since they were allowed to cool down to 40 K, eventually the outer disks in the β cooling models became gravitationally unstable, whereas that was prohibited for the FLD models. Comparing the final density distributions in Figures 2 and 3 with those for the β cooling models in Boss (2021; Figures 2 and 3) shows that the spiral arms in the latter models extend to the outer grid boundary, but are considerably more restricted to the inner disk in the present models. Clearly this explains the difference in semi-major axes seen in Figure 5. Also shown for comparison are the exoplanets listed in the Extrasolar Planets Encyclopedia for masses between 0.1 and 5 M_{Jup} and semi-major axes between 4 au and 20 au. Exoplanet demographics is an active and ongoing area of research, and the present models suggest that there may be significant numbers of gas giants orbiting beyond 5 au, as in the models of Boss (2017, 2019, 2021), awaiting detection.

Figure 6 again compares the results between the present FLD models and the β cooling models of Boss (2021). As in Figure 5, clumps in the latter models formed at significantly larger orbital distances, though their orbits have eccentricities quite similar to those of the FLD models, with most eccentricities falling below ~ 0.15 . Clearly with quadrupled spatial resolution, the present models, as well as those of Boss (2021), appear to predict similar initial masses and eccentricities, though the semi-major axes differ significantly for known reasons.

Another comparison is to Boss (2017), where the same radial temperature constraint was applied as in the present models. Boss (2017) also used the β cooling approximation for disks with a wide range of β values (1 to 100), starting with initial disks ranging from Toomre $Q_{min} = 1.3$ to $Q_{min} = 2.7$. The spatial resolution of Boss (2017) was limited to no more than

$N_r = 200$ and $N_\phi = 1024$, but otherwise the comparison between the present FLD models and the β cooling models is appropriate. Figure 7 shows the total number of clumps and VPs from Table 1 for the present FLD models, compared to the total numbers of VPs found in the β cooling models of Boss (2017). Figure 7 shows that the $\beta = 1, 3,$ and 10 results span the results for the present FLD models, while the $\beta = 100$ results do not match as well. None of these four β values matches the FLD results exactly. This implies a simple single value for β does not do justice to representing the FLD results, though the inherent stochasticity of the disk gravitational instability mechanism makes drawing any firmer conclusion impossible. Given this observation, Figure 7 indicates that β cooling parameters in the range of ~ 1 to ~ 10 seem to be supported by the FLD models, straddling the midpoint critical value of $\beta = 3$ first suggested by Gammie (2001).

Determining whether or not there is a correct critical β value for fragmentation continues to be controversial, as discussed by Boss (2017, 2019) and others. E.g., Meru & Bate (2011b) studied convergence with an SPH code with as many as 16,000,000 particles, and found that fragmentation occurred for larger β values as the resolution was increased, leading to doubt whether a critical value of β exists. Meru & Bate (2011a) found that estimates of a critical β depend on the assumed underlying disk density profile and argued against the generality of a specific critical β value. On the other hand, Baehr et al. (2017) used local three-dimensional disk simulations to find a critical $\beta \sim 3$. Differences in the numerical model, such as global vs. local, radiative transfer scheme, gravitational potential solver, spatial grid resolution (as reviewed by Durisen et al. 2007; Helled et al. 2014), and in the initial disk model, such as the initial density and temperature distributions (Boss 2017), make it difficult, if not impossible, for a valid comparison of the results on critical values of β obtained by different groups.

Nevertheless, the Figure 7 results are similar to those of Mercer et al. (2018), who used two approximate radiative transfer procedures to show that the effective value of β could vary from ~ 0.1 to ~ 200 , i.e., a single, constant value of β may not be appropriate. This suggests that more physically based cooling approximations than constant in space and time β should be investigated. E.g., Baehr & Klahr (2015) employed a definition for cooling that depended on a number of factors, such as the midplane temperature and sound speed, the disk surface density, the Rosseland mean opacity, and the local angular velocity.

Boss (2008, 2012) also calculated FLD models of disk instability. However, the Boss (2008) study was limited to using the flux-limiter version of the EDTONS code to continue the evolution of a previous model that did not use a flux-limiter, in order to discern what effect the flux-limiter might be found to have. After about 8 yr of FLD evolution, the FLD disks were found to have significantly hotter midplane temperatures, but clump formation was still able to proceed. Boss (2012) presented three models where the FLD code was used

from the start of the evolution, and found that clump formation was still likely. However, these latter models were restricted to abbreviated evolutions of only ~ 65 yr and to relatively low spatial resolution ($N_r = 100$ and $N_\phi = 512$). Thus the present models, enabled by the computational power of the memex cluster, provide a much more authoritative analysis of FLD models of gas disk gravitational instability.

Mayer et al. (2007) presented the first 3D SPH models of disk instability that included radiative transfer in the flux-limited diffusion approximation. Their initial disks were similar to those of the present model fldA, extending from 4 au to 20 au around a solar-mass protostar, with outer disk temperatures of 40 K and masses of $\sim 0.1M_\odot$. Their Figure 1 shows the results of several disks that fragmented and formed $\sim M_{Jup}$ clumps orbiting between ~ 5 au and ~ 10 au, a result quite similar to that of the present models (cf. Figure 5). The Mayer et al. (2007) models used 10^6 SPH particles, compared to the total of 3.6864×10^7 grid cells in the present calculations at their highest spatial resolution.

Meru & Bate (2010, 2011a) also presented FLD SPH models of disk instabilities, starting with 25 au-radius disks of mass $\sim 0.1M_\odot$ orbiting solar-mass protostars. With 2.5×10^5 particles, they found that clumps formed from ~ 5 au out as far as ~ 20 au, somewhat larger distances than found in the present FLD models (Figure 5, blue points) or the Mayer et al. (2007) models, but similar to the clump distances obtained in the β cooling models of Boss (2021), as can also be seen in Figure 5 (red points). The Meru & Bate (2010, 2011a) models started with an initial Toomre Q profile that fell to a minimum value of ~ 2 at 24 au, compared to the present models, where the minimum Toomre Q value is reached just beyond ~ 10 au. Given equivalent Q values, clumps will form faster in regions closer to the protostar, where the orbital period is shorter, explaining the slight differences with the Meru & Bate (2010, 2011a) FLD results.

Finally, note that the large-scale ring that formed in model fldH (Figure 3) did not lead to clump formation, but could still play an important role in gas giant planet formation. Such a gas disk ring provides a gas pressure bump that can lead to the rapid orbital aggregation of small solids toward the center of the ring, caused by gas disk headwinds for particles on orbits beyond that of the ring and tail winds for orbits interior to the ring’s orbit (Haghighipour & Boss 2003). Such a pressure bump could hasten the pebble accretion mechanism for gas giant planet formation at large distances (Chambers 2021). Such a situation implies that hybrid models of gas giant planet formation, involving both collisional accumulation and gravitationally unstable gas disks, should be investigated as thoroughly as the two end member mechanisms.

6. Conclusions

The flux-limited diffusion approximation provides a formally more accurate handling of gas disk thermodynamics, coupled with detailed equations of state and Rosseland mean opacities, as is the case for the present set of models, compared to the β cooling approximation. The spatial resolution in these new models, effectively equal to a hydrodynamical grid with as many as 3.6×10^7 spherical coordinate grid points, is unprecedented for EDTONS FLD models, and the continued robustness of the dense clump formation process in suitably unstable disks supports the disk instability mechanism for gas giant protoplanet formation as the continuum limit is approached. Compared to previous β cooling models, the results suggest that $\beta \sim 3$ produces similar numbers of clumps as the FLD models. If such clumps continue to contract and survive their subsequent orbital evolution, these FLD models, coupled with the previous β cooling models, imply that significant numbers of Jupiter-mass exoplanets may orbit at distances that are not well-sampled by ground- or space-based telescopic surveys to date. However, the Roman Space Telescope, scheduled for launch in 2026, has the ability to detect these exoplanets through its gravitational microlensing survey. A few might even be directly imaged with Roman’s coronagraphic instrument (CGI).

The computations were performed on the Carnegie Institution memex computer cluster (hpc.carnegiescience.edu) with the support of the Carnegie Scientific Computing Committee. I thank Floyd Fayton for his invaluable assistance with the use of memex and the referee for several suggestions for improving the manuscript.

REFERENCES

- Adibekyan, V. 2019, *Geosciences*, 9, 105
- Baehr, H., & Klahr, H. 2019, *ApJ*, 881, 162
- Baehr, H., Klahr, H., & Kratter, K. M. 2017, *ApJ*, 848, 40
- Bodenheimer, P., Yorke, H. W., Różyczka, M., Tohline, J. E., 1990, *ApJ*, 355, 651
- Boley, A. C., Hayfield, T., Mayer, L., & Durisen, R. H. 2010, *Icarus*, 207, 509
- Borucki, W. J., Koch, D., Basri, G., et al. 2010, *Sci*, 327, 977
- Boss, A. P. 1984, *ApJ*, 277, 768
- Boss, A. P. 1993, *ApJ*, 417, 351
- Boss, A. P. 1997, *Science*, 276, 1836
- Boss, A. P. 2001, *ApJ*, 563, 367

- Boss, A. P. 2005, *ApJ*, 629, 535
- Boss, A. P. 2007, *ApJL*, 661, L73
- Boss, A. P. 2008, *MNRAS*, 419, 1930
- Boss, A. P. 2009, *ApJ*, 694, 107
- Boss, A. P. 2012, *ApJ*, 677, 607
- Boss, A. P. 2013, *ApJ*, 764, 194
- Boss, A. P. 2017, *ApJ*, 836, 53
- Boss, A. P. 2019, *ApJ*, 884, 56
- Boss, A. P. 2021, *ApJ*, 911, 146
- Boss, A. P., & Myhill, E. A. 1992, *ApJS*, 83, 311
- Boss, A. P., Fisher, R. T., Klein, R. I., & McKee, C. F. 2000, *ApJ*, 528, 325
- Brucy, N., & Hennebelle, P. 2021, *MNRAS*, 503, 4192
- Bryson, S., Kunimoto, M., Kopparapu, R. K. , et al. 2021, *AJ*, 161, 36
- Chambers, J. 2018, *ApJ*, 865, 30
- Chambers, J. 2021, *ApJ*, 914, 102
- Deng, H., Mayer, L. , & Helled, R. 2021, *Nature Astronomy*, 5, 440
- Durisen, R. H., Boss, A. P., Mayer, L., Nelson, A., Rice, K., & Quinn, T. R. 2007, in *Protostars and Planets V*, ed. B. Reipurth, D. Jewitt, & K. Keil (Tucson, AZ: Univ. Arizona Press), 607
- Fryxell, B., Olson, K., Ricker, P., et al. 2000, *ApJS*, 131, 273
- Fulton, B. J., Rosenthal, L. J., Hirsch, L. A., et al. 2021, *ApJS*, 255, 14
- Gammie, C. F. 2001, *ApJ*, 553, 174
- Haghighipour, N., & Boss, A. P. 2003, *ApJ*, 583, 996
- Helled, R., Bodenheimer, P., Alibert Y., et al. 2014, in *Protostars & Planets VI*, eds. H. Beuther, R. Klessen, K. Dullemond, and Th. Henning, 643
- Koch, D. G., Borucki, W. J., Basri, G., et al. 2010, *ApJ*, 713, L79
- Kunimoto, M., & Matthews, J. M. 2020, *AJ*, 159, 248.
- Levermore, C. D., & Pomraning, G. C. 1981, *ApJ*, 248, 321
- Matsumura, S., Brasser, R., & Ida, S. 2021, *A&A*, 650, A116
- Mayer, L., Lufkin, G., Quinn, T., & Wadsley, J. 2007, *ApJ*, 661, L77

- Mercer, A., Stamatellos, D., & Dunhill, A. 2018, MNRAS, 478, 3478
- Meru, F., & Bate, M. R. 2010, MNRAS, 406, 2279
- Meru, F., & Bate, M. R. 2011a, MNRAS, 410, 559
- Meru, F., & Bate, M. R. 2011b, MNRAS, 411, L1
- Mishenina, T., Basak, N., Adibekyan, V., Soubiran, C., & Kovtyukh, V. 2021, MNRAS, 504, 4252
- Mizuno, H. 1980, Prog. Theor. Phys., 64, 544
- Nelson, A. F. 2006, MNRAS, 373, 1039
- Ruffert, M., & Arnett, D. 1994, ApJ, 427, 351
- Szulágyi, J., Mayer, L., & Quinn, T. 2017, MNRAS, 464, 3158
- Wetherill, G. W. 1990, AREPS, 18, 205
- Wetherill, G. W. 1996, Icarus, 119, 219
- Yamamoto, Y., Okamoto, T., & Saitoh, T. R. 2021, MNRAS, 504, 3986
- Yang, C. C., Johansen, A., & Carrera, D. 2017, A&A, 606, A80
- Youdin, A. N., & Goodman, J. 2005, ApJ, 620, 459

Table 1. Initial conditions and final results for the eight new FLD models with up to quadrupled spatial resolution in both the radial and azimuthal spherical coordinates compared to Boss (2008, 2012), showing the initial outer disk temperatures (T_{oi}), initial minimum Toomre Q_{min} , the final time, final numbers of radial and azimuthal grid points, the number of VPs and of viable clumps at the final time, and the sum of those two ($N_{VP} + N_{clumps} = N_{total}$).

Model	T_{oi} (K)	Q_{min}	final time (yrs)	final N_r	final N_ϕ	N_{VP}	N_{clumps}	N_{total}
fldA	40	1.3	189.	400	2048	3	5	8
fldB	60	1.6	253.	400	2048	2	1	3
fldC	70	1.7	260.	400	2048	0	3	3
fldD	80	1.9	307.	400	2048	0	3	3
fldE	90	2.0	313.	400	1024	0	0	0
fldF	100	2.1	287.	400	2048	1	0	1
fldG	120	2.2	504.	200	1024	0	1	1
fldH	180	2.7	1822.	100	512	0	0	0

Table 2. Results for the new models, showing the estimated properties for the densest clumps present at the final times of the models, classified as either unbound (U), weakly (W), or strongly (S) self-gravitating, based on whether the clump mass is less than (U), greater than (W), or more than 1.5 times (S) the Jeans mass for self-gravitational collapse, with implications for clump survival.

Model	Q_{min}	clump #	ρ_{max} (g cm ⁻³)	M_{clump}/M_{Jup}	$T_{average}$ (K)	M_{Jeans}/M_{Jup}	status
fldA	1.3	1	1.8×10^{-9}	0.556	73.0	0.477	W
fldA	1.3	2	1.0×10^{-9}	0.699	53.3	0.498	W
fldA	1.3	3	3.9×10^{-10}	1.28	50.5	0.651	S
fldA	1.3	4	7.8×10^{-10}	0.845	53.3	0.542	S
fldA	1.3	5	1.3×10^{-9}	0.651	54.4	0.414	S
fldB	1.6	1	9.47×10^{-9}	0.854	62.5	0.194	S
fldB	1.6	2	7.13×10^{-10}	0.946	124.	2.01	U
fldB	1.6	3	2.27×10^{-9}	1.18	130.	1.24	U
fldB	1.6	4	6.47×10^{-10}	0.717	90.9	1.13	U
fldC	1.7	1	1.38×10^{-9}	1.10	92.5	0.868	W
fldC	1.7	2	2.80×10^{-9}	1.21	74.4	0.482	S
fldC	1.7	3	1.47×10^{-9}	0.835	70.1	0.523	S
fldD	1.9	1	5.02×10^{-9}	0.827	80.0	0.384	S
fldD	1.9	2	8.53×10^{-10}	1.13	82.8	0.957	W
fldD	1.9	3	7.71×10^{-10}	1.90	81.9	1.05	S
fldD	1.9	4	3.69×10^{-10}	1.14	140.	3.09	U
fldE	2.0	1	5.05×10^{-10}	0.736	90.5	1.34	U
fldF	2.1	0	–	–	–	–	–
fldG	2.2	1	2.03×10^{-9}	3.69	135.	1.29	S
fldH	2.7	0	–	–	–	–	–

Table 3. Masses and orbital parameters for the gravitationally bound clumps, i.e., those with a status of W or S in Table 2, as well as for the VPs, both at the final times listed in Table 1.

Model	Q_{min}	clump #	VP #	M/M_{Jup}	semimajor axis (au)	eccentricity	status
fldA	1.3	1	–	0.556	8.62	0.101	W
fldA	1.3	2	–	0.699	10.35	0.111	W
fldA	1.3	3	–	1.28	10.37	0.037	S
fldA	1.3	4	–	0.845	10.91	0.053	S
fldA	1.3	5	–	0.651	8.23	0.117	S
fldA	1.3	–	1	0.31	8.34	0.057	–
fldA	1.3	–	2	0.023	7.38	0.140	–
fldA	1.3	–	3	0.92	5.42	0.123	–
fldB	1.6	1	–	0.854	9.98	0.141	S
fldB	1.6	–	1	0.515	4.73	0.505	–
fldB	1.6	–	2	0.540	–	–	unbound
fldC	1.7	1	–	1.10	8.86	0.136	W
fldC	1.7	2	–	1.21	7.44	0.0558	S
fldC	1.7	3	–	0.835	9.56	0.108	S
fldD	1.9	1	–	0.827	8.49	0.0698	S
fldD	1.9	2	–	1.13	10.5	0.0514	W
fldD	1.9	3	–	1.90	10.7	0.0813	S
fldE	2.0	–	–	–	–	–	–
fldF	2.1	–	1	0.750	5.06	0.154	–
fldG	2.2	1	–	3.69	8.58	0.155	S
fldH	2.7	–	–	–	–	–	–

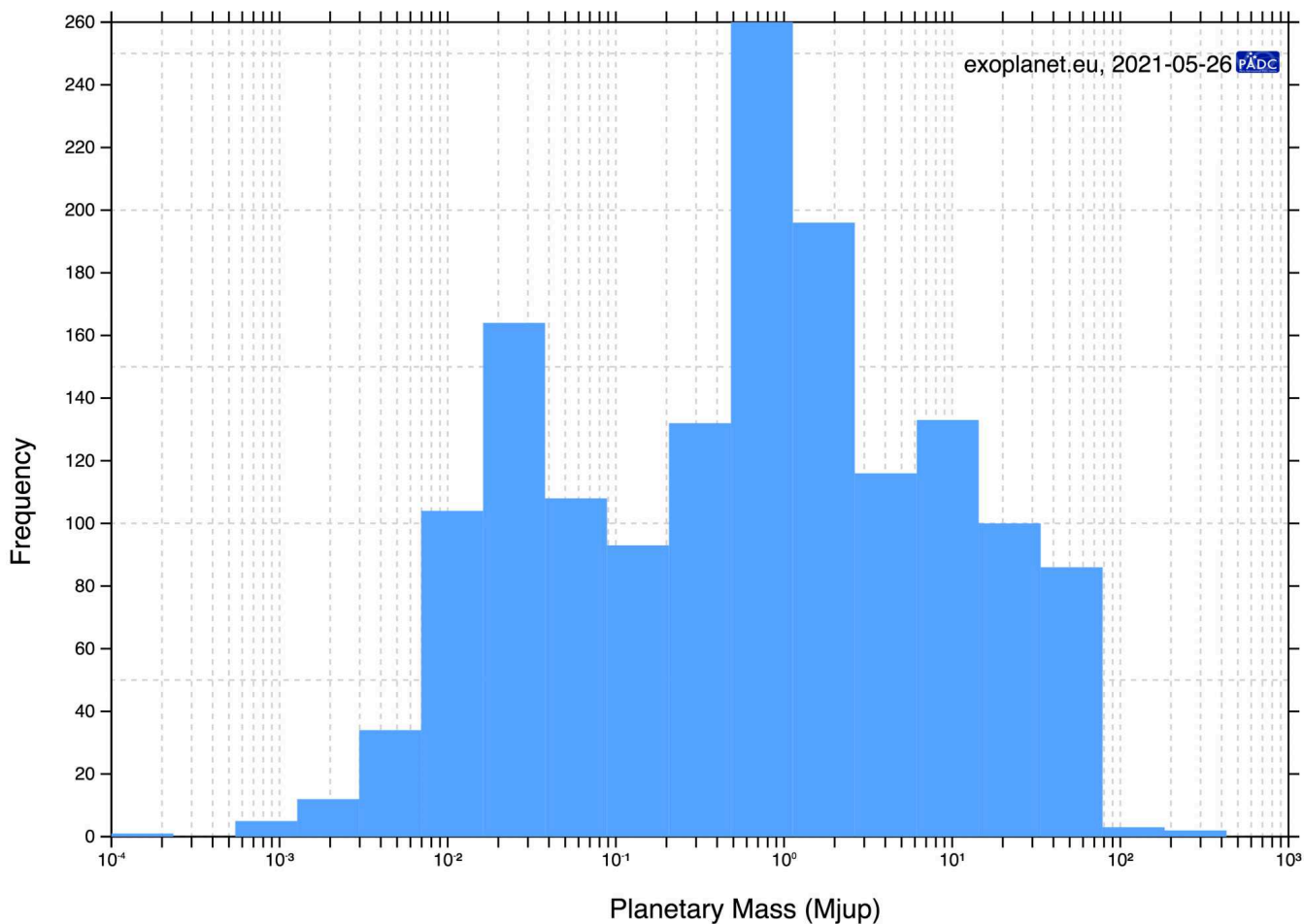


Fig. 1.— Frequency of planets in the Extrasolar Planets Encyclopedia database (exoplanet.eu) as a function of planetary mass for confirmed mass planets ranging between $10^{-4}M_{Jup}$ and 10^3M_{Jup} . Super-Earths and sub-Neptunes with masses of $\sim 2 \times 10^{-2}M_{Jup}$ represent one peak in the distribution, while Jupiter-mass gas giants represent an even higher peak, largely as a result of the relative ease of their detection.

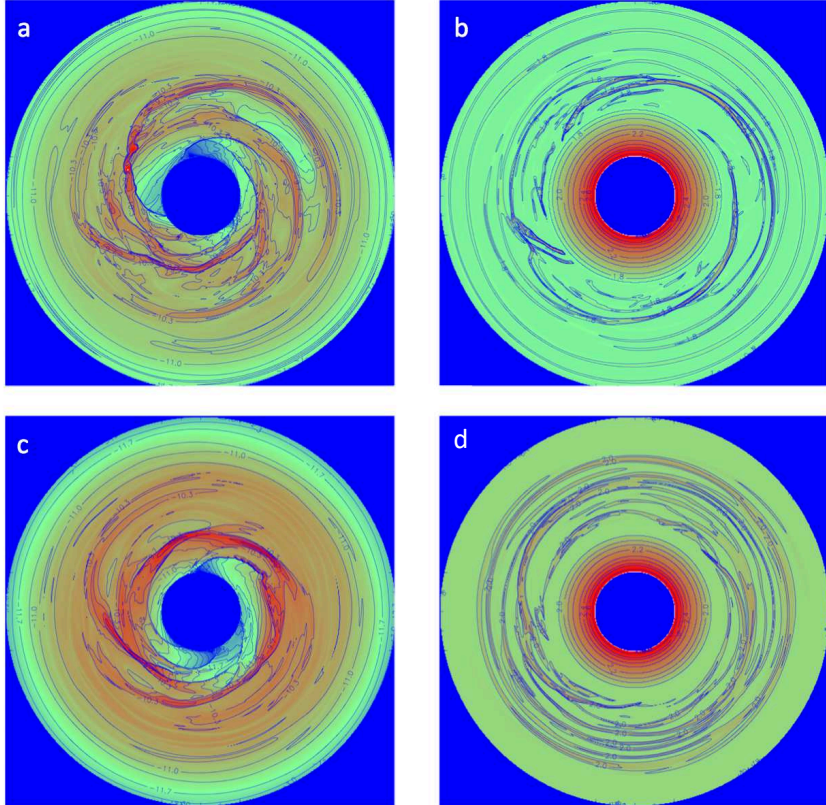


Fig. 2.— Equatorial (midplane) density (left) and temperature (right) contours for models fldA (a,b) at 189 yrs and for model fldC (c,d) at 260 yrs, respectively. The disks have inner radii of 4 au and outer radii of 20 au. Density contours are labelled in log cgs units and temperature contours are labelled in log K units. Maximum midplane gas densities are: (a) $1.35 \times 10^{-8} \text{ g cm}^{-3}$ and (c) $3.31 \times 10^{-9} \text{ g cm}^{-3}$. The initial maximum midplane density is $1.0 \times 10^{-10} \text{ g cm}^{-3}$ at 4 au. The models start with initial outer disk temperatures ranging from 40 K (light green color) for model fldA to 180 K (light orange color) for model fldH. Red colors correspond to temperatures of $\sim 600 \text{ K}$ close to the inner boundary.

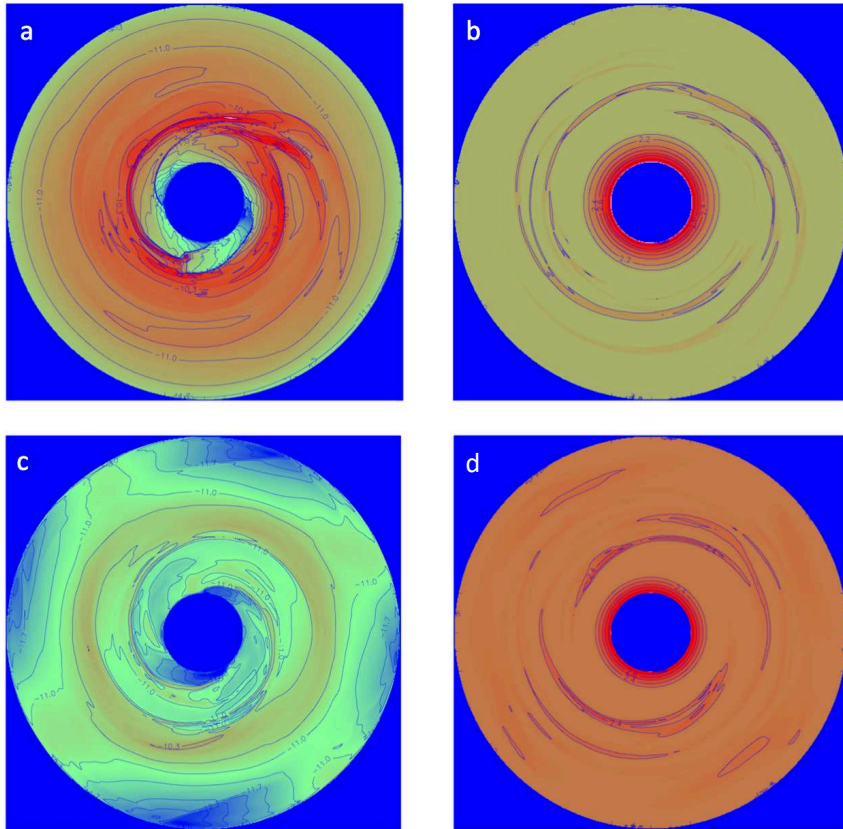


Fig. 3.— Equatorial (midplane) density (left) and temperature (right) contours for models fldF (a,b) at 287 yrs and for model fldH (c,d) at 1822 yrs, respectively, plotted as in Figure 2. Maximum midplane gas densities are: (a) $8.71 \times 10^{-10} \text{ g cm}^{-3}$ and (c) $5.01 \times 10^{-11} \text{ g cm}^{-3}$.

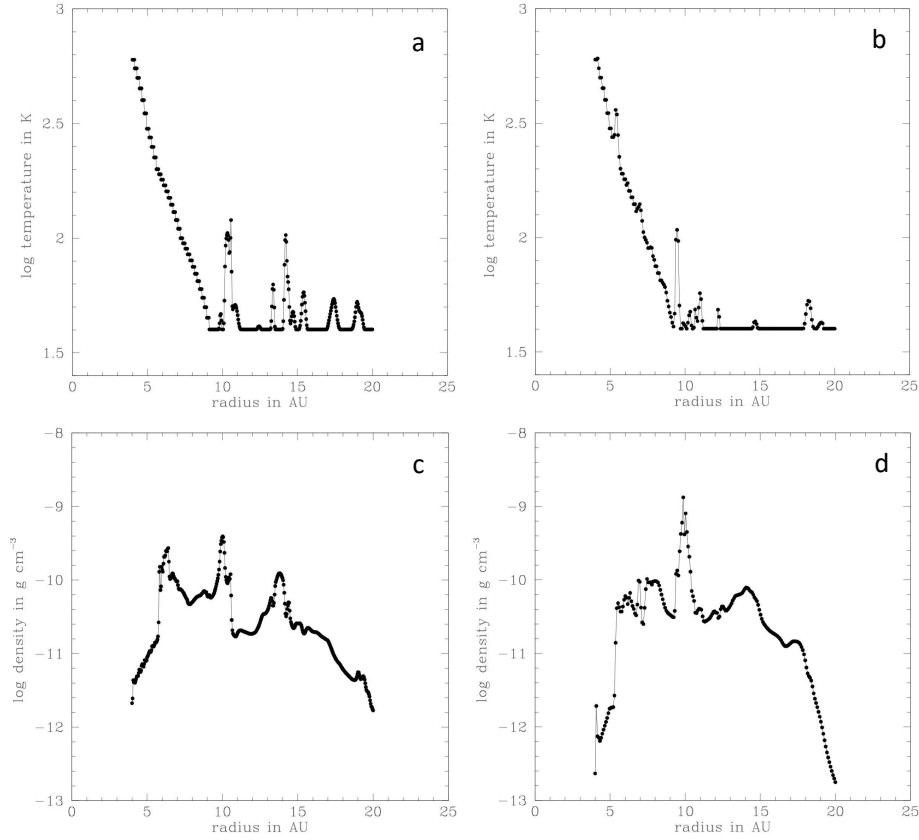


Fig. 4.— Radial temperature (a) and density (c) profiles through a representative FLD model highlighting the model fldA clump 3 (Table 1), seen at about 3 o’clock in Figure 2 at an orbital distance of ~ 10 au, compared to a representative clump (b, d) at a similar time of evolution (174 yr) from model 1.3-3 (Table 1 in Boss 2017), where $\beta = 3$ cooling was used rather than the flux-limited diffusion approximation. In both cases the clumps orbit at ~ 10 au and are defined by sharply peaked profiles in both the midplane density and the temperature fields.

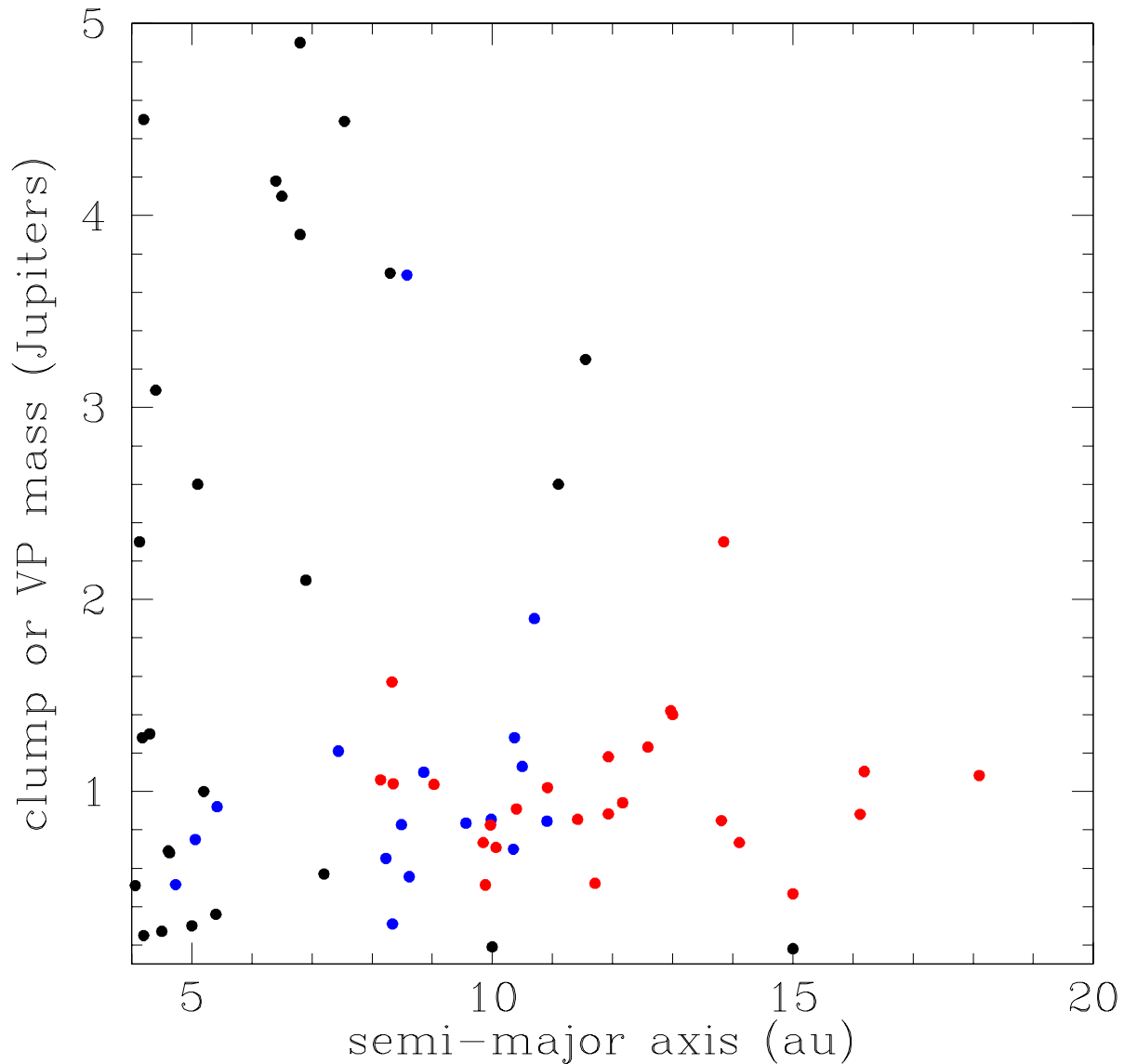


Fig. 5.— Masses and semi-major axes of the gravitationally bound clumps and VPs from Table 3 are shown in blue, while the red points show the gravitationally bound clumps from Boss (2021), where β cooling was used rather than the flux-limited diffusion approximation. The black points show all exoplanets listed in the Extrasolar Planets Encyclopedia (exoplanets.eu) for masses between 0.1 and 5 M_{Jup} and semi-major axes between 4 au and 20 au.

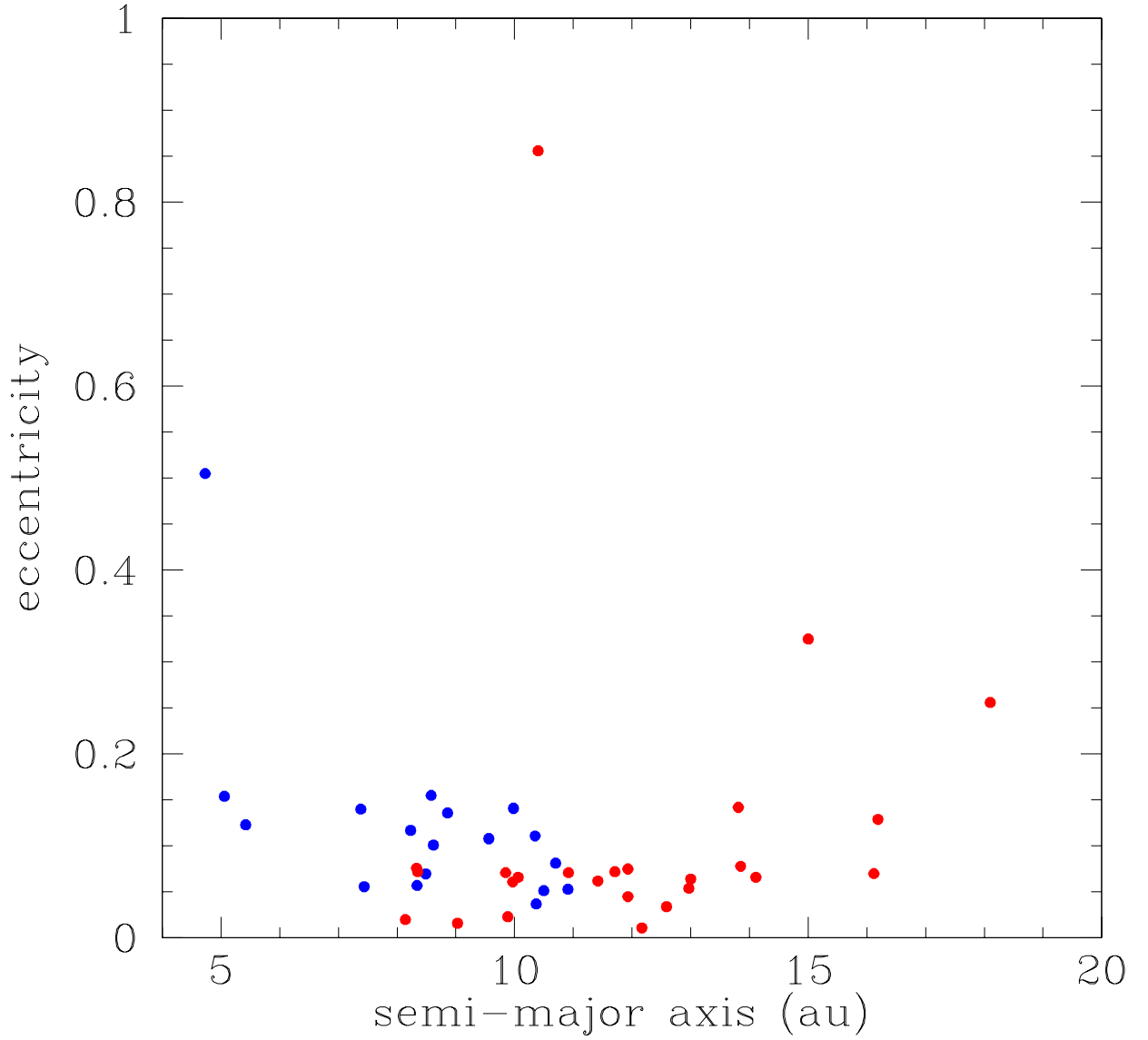


Fig. 6.— Eccentricities and semi-major axes for the gravitationally bound clumps and VPs listed in Table 3 are shown in blue, while the red points show the gravitationally bound clumps from Boss (2021), where β cooling was used rather than the flux-limited diffusion approximation.

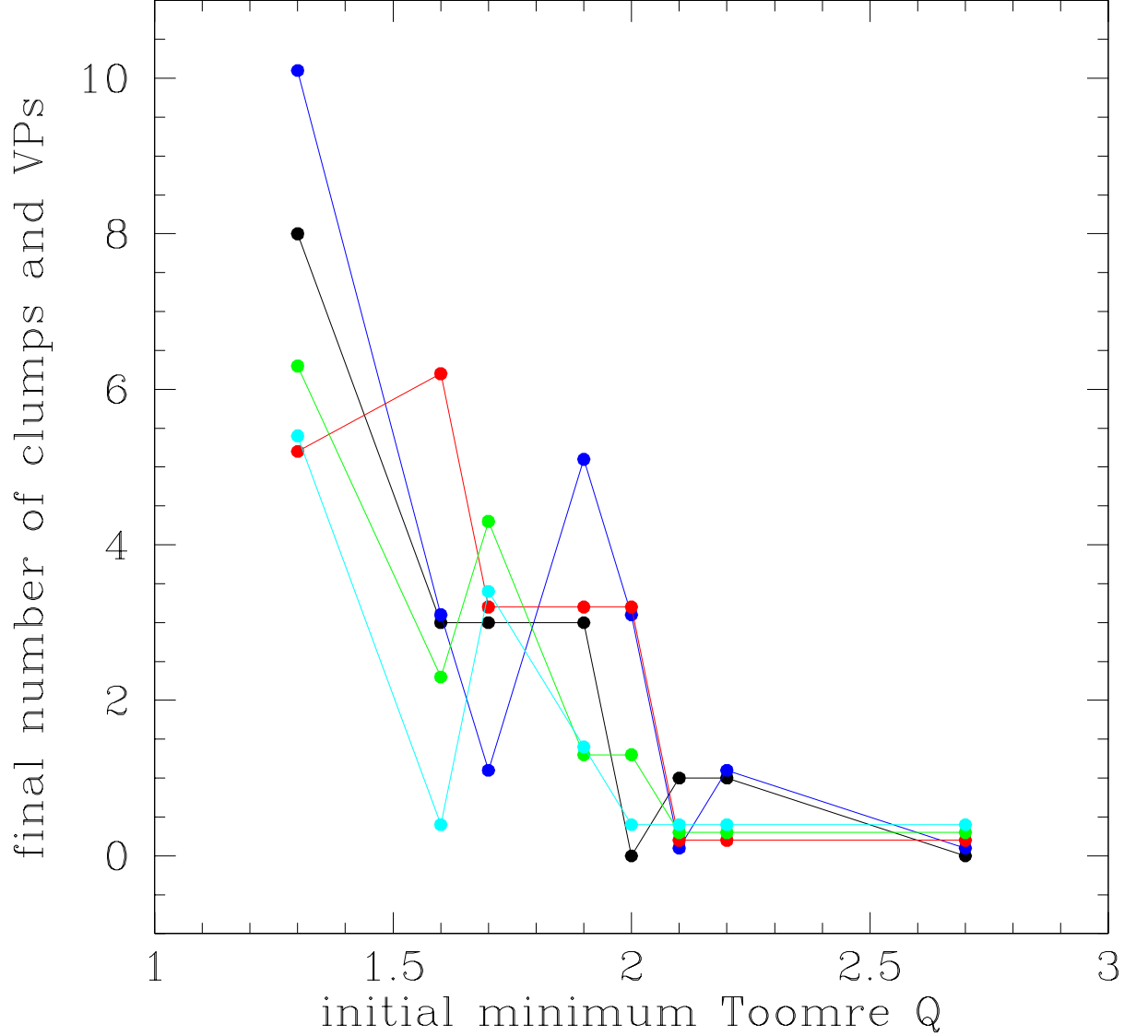


Fig. 7.— Black points and connecting lines plot the total number of clumps and VPs from Table 1 for the present eight FLD models, each starting with a different initial outer disk temperature and hence with a different initial minimum Q , while the four other colors represent the total numbers of VPs found in the equivalent initial minimum Q β cooling model of Boss (2017), with blue for $\beta = 1$, red for $\beta = 3$, green for $\beta = 10$, and cyan for $\beta = 100$. The VP numbers for the colored points are adjusted upwards by 0.1 for each increase in β for clarity.